Reaction mechanisms involving weakly bound ^{6}Li and ^{209}Bi at energies near the Coulomb barrier

S. Santra,* S. Kailas, K. Ramachandran, V. V. Parkar,† V. Jha, B. J. Roy, and P. Shukla
Nuclear Physics Division, Bhabha Atomic Research Centre, Mumbai 400085, India
(Received 19 November 2010; revised manuscript received 1 March 2011; published 28 March 2011)

The elastic, inelastic, and transfer cross sections are measured for the ^{6}Li + ^{209}Bi reaction at energies around the Coulomb barrier. The optical model analysis of elastic scattering shows a breakup threshold anomaly in the energy dependence of the real and imaginary potentials. The observed energy dependence is found to be consistent with the dynamic polarization potential obtained from the coupled-channels calculations that explain the above measured reaction channels simultaneously. A comparison of different reaction probabilities reveals that the relative contribution of breakup starts increasing at energies below the Coulomb barrier, in contrast to the behavior of other reaction channels, which get closed as energy is lowered. The large probability of projectile breakup at sub-Coulomb energies leads to the observation of a nonzero imaginary potential even at $E_{\rm lab} \leqslant 0.8V_B$.

DOI: 10.1103/PhysRevC.83.034616 PACS number(s): 25.70.Bc, 25.70.Hi, 25.70.Jj

I. INTRODUCTION

The effect of coupling between the relative motion and the intrinsic degrees of freedom of the participating nuclei is manifested as a "threshold anomaly" in the energy-dependence behavior of the real part of the effective interaction potential [1]. Although this behavior is observed for most of the reactions involving strongly bound stable projectiles, for example, ^{12}C + ^{208}Pb,^{209}Bi [2,3], it may not be true for the reactions involving loosely bound projectiles with large breakup probability, for example, ^{6}Li + ^{208}Pb [4], ^{6}Li + ^{138}Ba [5], ^{6}Li + ^{59}Co [6], ^{6}Li + ^{28}Si [7], ^{9}Be + ^{209}Bi [8], and ^{9}Be + ^{64}Zn [9,10]. For the latter systems, there is no pronounced energy dependence of the real potential, and at energies below the Coulomb barrier the imaginary potential is found to remain constant or sometimes increases with decreasing energy. The increase in the imaginary potential below the Coulomb barrier is sometimes associated with a slight decrease in the real potential. Hussein *et al.* have showed that this behavior is a new manifestation of the dispersion relation and named it the "breakup threshold anomaly" [11].

Though no threshold anomaly is observed in many reactions involving ^{6}Li and ^{9}Be [4–10], it still exists for ^{7}Li [4–7]. Since breakup thresholds of ^{6}Li ($E_{\alpha d}$ = 1.48 MeV) and ^{9}Be ($E_{\alpha\alpha n}$ = 1.57 MeV) are similar and lower than that of ^{7}Li ($E_{\alpha t}$ = 2.47 MeV), it can be understood that the large breakup probabilities of ^{6}Li and ^{9}Be may be affecting the traditional energy dependence of the real potential. In addition to the larger breakup threshold (2.47 MeV) of ^{7}Li, it has a bound excited state at 0.478 MeV, which is much lower than its breakup threshold. The effect of coupling of this inelastic state to elastic scattering may still be manifested in the optical model (OM) potential as the normal threshold anomaly. However, contradictory results exist involving same weakly bound projectiles: e.g., Signorini *et al.* did not observe any threshold anomaly for ^{9}Be + ^{209}Bi [8], while Woolliscroft *et al.* saw a pronounced threshold anomaly for a very similar system, ^{9}Be + ^{208}Pb [12]. This implies that a clear understanding of the effect of breakup on the energy dependence of the optical potential is still elusive. Systematic studies of more reactions involving weakly bound projectiles are necessary to unfold these effects.

Since the breakup is one of the reaction channels, its coupling with the elastic channel may lead to enhancement of complete fusion (CF), exhibiting the threshold anomaly. Alternatively, the breakup of the projectile before reaching the fusion barrier will lead to loss of flux and hence the CF should be reduced [13]. Thus the coupling mechanism will be best understood when the same set of potential parameters are used in the coupled-channels calculations to understand both the elastic and the fusion data simultaneously. In addition, if the couplings and potential parameters are unique then coupled-channels (CC) calculations are expected to reproduce the cross sections for other nonelastic channels too. This is a challenging task because one needs (i) to measure the cross sections for all the above channels and (ii) to find a unique parameter set that describes them through the same CC calculations.

Since both the CF and ICF (incomplete fusion) cross sections for the ^{6}Li + ^{209}Bi system at energies around the Coulomb barrier, $V_B \simeq$ 30 MeV (in the center of mass), are available in the literature [14], we chose this reaction for the present study. To have a complete set of data, we decided to measure the elastic, inelastic, and transfer cross sections for the same system. Earlier we have already measured the exclusive breakup of ^{6}Li $\rightarrow \alpha + d$ at $E_{\rm lab}$ = 36 and 40 MeV for the above system [15]; this will act as an additional constraint in the coupled-channels calculations. In a very recent work by A. Gomez Camacho *et al.* on ^{6,7}Li + ^{28}Si [16], a simultaneous description of the elastic, fusion, and reaction cross sections has been made, where the nuclear polarization potential is split into a volume part and a surface part to understand the energy dependence of the OM potential in terms of different polarization potentials. It would be interesting to see whether a simultaneous description of all the channels as well as the energy dependence of the OM potential is possible for the present system (^{6}Li + ^{209}Bi) through the same CC calculations

*ssantra@barc.gov.in
†Present address: Departamento de Física Aplicada, Universidad de Huelva, E-21071 Huelva, Spain.

with a large amount of experimental data for inelastic, transfer, and fusion channels as constraints. It would also be interesting to compare the probabilities of different reaction channels involved in the present reaction and understand the effect of projectile breakup on elastic and fusion cross sections.

In this paper, we present the results of the measurements and analysis of elastic, inelastic, and transfer cross sections for the ^{6}Li + ^{209}Bi system. Details of the measurements are given in Sec. II. The optical model data analysis of elastic scattering, the coupled-channels calculations, and the results are discussed in Sec. III. Finally, the results are summarized in Sec. IV.

II. MEASUREMENTS

The experiment was performed using a ^{6}Li beam from the BARC-TIFR 14-UD pelletron facility in Mumbai. The self-supporting target (^{209}Bi), with a thickness of ~330 μg/cm^2, was prepared by the vacuum evaporation technique. Four ΔE-E telescopes of Si surface barrier detectors were placed 10° apart on a movable arm inside a 1-m-diameter scattering chamber to catch the projectile-like fragments. Each telescope, with a 5-mm-diameter collimator, has an angular opening of ±0.5°. The telescopes, with detector thicknesses of ΔE = 25–33 μm and E = 500–1000 μm, were suitable for detection of particles with Z = 1, 2, and 3. Two monitors of single-surface barrier detectors of 2000 μm thickness were placed at ±25° on either side of the beam for cross-section normalization and beam monitoring.

A typical two-dimensional spectrum and the one-dimensional projections for ^{7}Li and ^{6}Li particles detected by a telescope at θ_{lab} = 100° for E_{beam} = 38 MeV are shown in Fig. 1. A one-dimensional projection of ^{7}Li corresponding to the 1n pickup channel is shown in Fig. 1(b). The ^{7}Li$_1$ peak corresponds to the ground state of ^{7}Li and the ground state plus first excited state (0.063 MeV) of ^{208}Bi. ^{7}Li$_2$ corresponds to the ground state of ^{7}Li with the second excited state (0.51 MeV) of ^{208}Bi and the ground state of ^{208}Bi with the first excited state (0.478 MeV) of ^{7}Li. ^{7}Li$_3$ represents the first excited state (0.478 MeV) of ^{7}Li and the second excited state (0.51 MeV) of ^{208}Bi. Yields under only the ^{7}Li$_1$ peak were extracted and used for determining the cross sections and compared with the CC calculations. The elastic and target inelastic states (~2.6 MeV) corresponding to ^{208}Pb(3$^-$) $\bigotimes \pi h_{9/2}$ are clearly separated as shown in Fig. 1(c).

The elastic scattering angular distributions, measured in the angular range of θ_{lab} = 20°–173° at beam energies of E_{lab} = 24, 26, 28, 30, 32, 34, 36, 38, 40, and 50 MeV, including the data from Refs. [17,18] at 32.8 and 44 MeV, are shown in Fig. 2.

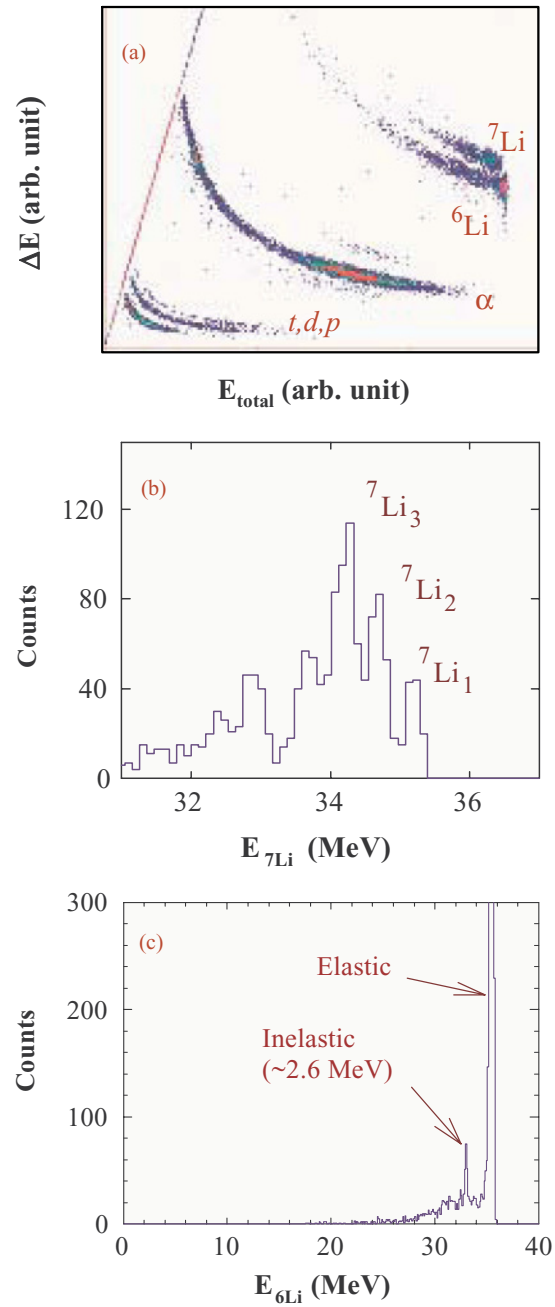

FIG. 1. (Color online) (a) A typical two-dimensional spectrum of ΔE vs E_{total} for ^{6}Li + ^{209}Bi measured by a telescope at θ_{lab} = 100° for E_{beam} = 38 MeV. Also shown are the one-dimensional projections for (b) ^{7}Li and (c) ^{6}Li. In (b), the ^{7}Li$_1$ peak corresponds to the ground state of ^{7}Li and the ground state plus first excited state of ^{208}Bi. ^{7}Li$_2$ and ^{7}Li$_3$ represent higher excited states of ^{7}Li and/or ^{208}Bi.

III. ANALYSIS AND DISCUSSION

A. Optical model analysis of elastic scattering

The measured elastic scattering angular distributions along with the data available in the literature [17,18] were analyzed by the optical model with a microscopic real potential [19], following the formalism described in Refs. [2,3]. The double-folded microscopic real potential V_F was calculated as

$$V_F = \int\int d\mathbf{r}_1 d\mathbf{r}_2 \rho(\mathbf{r}_1)\rho(\mathbf{r}_2)v(\mathbf{r}_{12}), \quad (1)$$

where $\mathbf{r}$ is the separation of the centers of mass of the two colliding nuclei, v is the effective nucleon-nucleon interaction, and the ρ's are point nucleon densities of ^{6}Li and ^{208}Pb. The

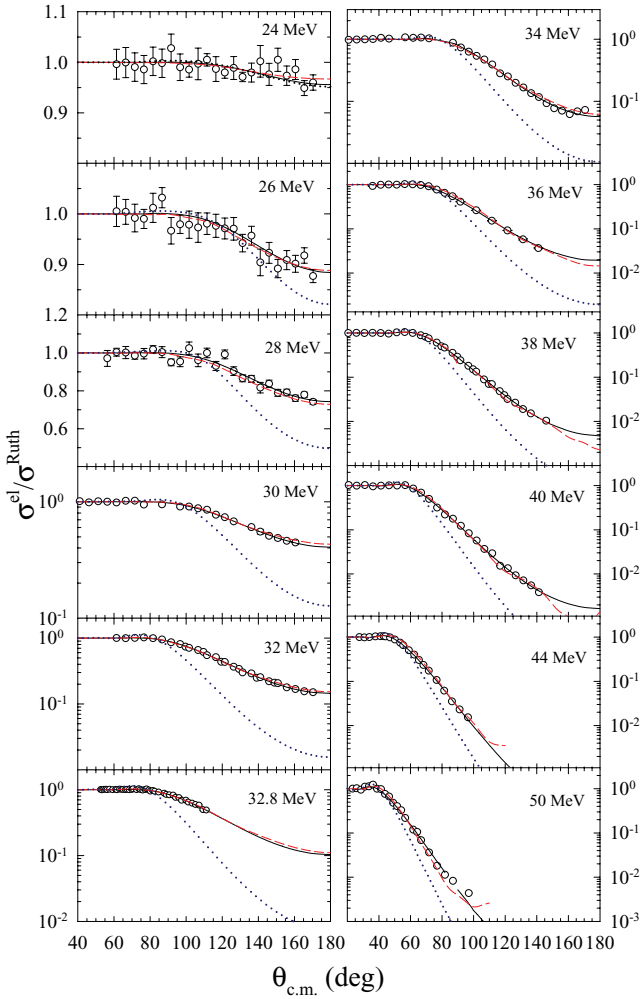

FIG. 2. (Color online) The elastic scattering angular distributions for ^{6}Li + ^{209}Bi at energies $E_{\rm lab}$ = 24–50 MeV, including the data from Refs. [17,18] at 32.8 and 44 MeV. Solid lines are the OM fit using the microscopic potential. Dashed (dotted) lines correspond to the CC calculations with full (no) couplings.

potentials were computed using the code DFPOT [20]. The interaction used was of the M3Y form [19], given by

$$v(r) = 7999\frac{e^{-4r}}{4r} - 2134\frac{e^{-2.5r}}{2.5r} + J_{00}\delta(r), \qquad (2)$$

where the third term accounts for knock-on exchange with $J_{00} = -265$ MeV fm^3. The charge density distribution is obtained by fitting the electron scattering data and is parametrized in the Fermi parabolic form [21],

$$\rho(r) = \frac{\rho_0(1 + wr^2/c^2)}{1 + \exp\left(\frac{r-c}{a}\right)}. \qquad (3)$$

The parameters used for the charge densities of ^{209}Bi (^{6}Li) are $c = 6.75$ (1.8736) fm, $a = 0.468$ (0.7533) fm, and $w = 0$ (-0.0236). The ρ_0 values were chosen so as to normalize the distribution to their respective charge numbers. The point nucleon densities were obtained from the charge densities after correcting for the finite size of the proton in the standard way [19], using the root-mean-square values of the radii, $\langle r^2\rangle^{\frac{1}{2}}$ = 2.56 and 5.51 fm, of ^{6}Li and ^{209}Bi, respectively.

The potential used to carry out the fits to the elastic scattering data was of the form

$$U(r) = -\lambda V_F(r) - iW(r) + V_c(r). \qquad (4)$$

The V_F potential was allowed an overall adjustable normalization coefficient λ to fit the elastic data at different energies. The imaginary part of optical potential was of Woods-Saxon form with its depth W_0, diffuseness a_w, and radius parameter r_w. The Coulomb potential, $V_c(r, r_c)$, was taken as that due to a uniformly charged sphere of radius $R_c = r_c(A_P^{1/3} + A_T^{1/3})$ with r_c fixed at 1.2 fm.

The best fits to the elastic scattering data were obtained by varying the parameters λ, W_0, and a_w. The radius parameter r_w was kept fixed at 1.2 fm. The resulting OM fits are shown as solid lines in Fig. 2. The parameters obtained from the fits to the experimental elastic scattering data at various energies are given in Table I. The errors on λ and W_0 are obtained by varying these parameters on either side of the best-fit values. The quoted errors are equal to the differences between the best-fit parameters (with minimum χ^2) and the values of the parameters where χ^2 increases by 15% above the minimum.

By using the best-fit parameters obtained from microscopic OM analysis, the real and imaginary potentials are calculated at the average strong absorption radius, $R_{\rm sa}$ = 12.4 fm. The strong absorption radius, at any energy, was computed from the formula for the distance of closest approach for the Coulomb trajectories, i.e.,

$$R_{\rm sa} = \frac{\eta}{k}\left[1 + \left(1 + \left(\frac{L_{\frac{1}{2}}}{\eta}\right)^2\right)^{\frac{1}{2}}\right]. \qquad (5)$$

Here, k is the wave number, η is the Sommerfeld parameter, and $L_{\frac{1}{2}}$ is the partial wave for which the transmission coefficient is 0.5, at the above energy. The mean value for $R_{\rm sa}$ was estimated to be 12.4 fm. By using the data from Table I the values of the real and the imaginary potentials are calculated at r = 12.4 fm and plotted as a function of bombarding energy in Fig. 3.

TABLE I. Optical model (microscopic) parameters from elastic scattering analysis. r_w was kept fixed at 1.2 fm.

$E_{\rm lab}$ (MeV)	λ	W_0 (MeV)	a_w (fm)	$\sigma_{\rm reac}$ (mb)
24	0.63 ± 1.38	29.77 ± 7.5	0.912	14.4
26	0.63 ± 0.51	48.44 ± 6.7	0.749	37.1
28	0.64 ± 0.16	28.59 ± 2.4	0.746	81
30	0.53 ± 0.05	35.92 ± 1.8	0.746	246
32	0.60 ± 0.03	37.92 ± 1.5	0.737	469
32.8	0.53 ± 0.05	31.62 ± 1.7	0.746	528
34	0.54 ± 0.02	26.74 ± 4.7	0.701	567
36	0.46 ± 0.03	39.42 ± 2.6	0.741	910
38	0.49 ± 0.02	27.44 ± 1.3	0.741	1015
40	0.60 ± 0.02	37.67 ± 2.5	0.700	1213
44	0.64 ± 0.02	32.79 ± 2.7	0.773	1608
50	0.68 ± 0.05	47.28 ± 7.6	0.700	1924

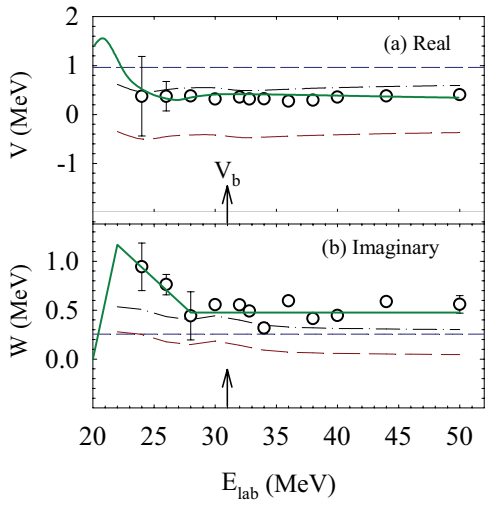

FIG. 3. (Color online) (a) The real and (b) the imaginary potentials (hollow circles) obtained from the OM analysis at strong absorption radius, $R_{sa} = 12.4$ fm. The solid lines are obtained from the dispersion relation. Results from the CC calculations for the real (imaginary) part of the bare potential V_{bare} (W_{bare}), dynamic polarization potential ΔV_p (ΔW_p), and effective potential, $V_{eff} = \Delta V_p + V_{bare}$ ($W_{eff} = \Delta W_p + W_{bare}$) are represented by short-dashed, medium-dashed, and dash-dotted lines, respectively.

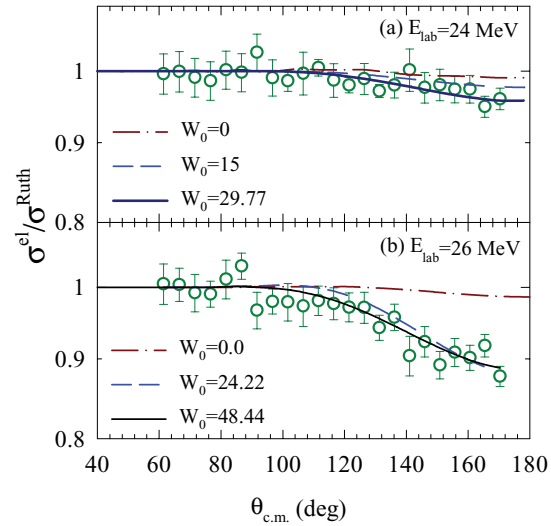

FIG. 4. (Color online) The elastic scattering calculated with different values of imaginary potential compared with the measured data to see the sensitivity. The solid line represents the best-fit values; the dash-dot and dashed lines correspond to the calculations with $W_0 = 0$ and an intermediate value, respectively.

The consistency between the real and the imaginary potentials (solid lines) was tested by a dispersion relation [22]. The imaginary part of the potential is represented in the form of three straight-line segments, as shown as solid lines in Fig. 3(b). The corresponding real part of the potential calculated from the dispersion relation is shown by a solid line in Fig. 3(a). From this it can be concluded that there is no pronounced energy dependence or "threshold anomaly" of the real potential (hollow circles) at energies around the Coulomb barrier, similar to the observations made earlier [4–6,8,10] for the reactions involving weakly bound ^{6}Li and ^{9}Be projectiles. As we go down in energy below the Coulomb barrier, the imaginary potential starts increasing (typical of the breakup threshold anomaly) and it does not vanish even at $E_{lab} \simeq 0.8 V_B$, indicating the presence of some open reaction channels.

To see the sensitivity of the imaginary potential at sub-barrier energies, the elastic scattering cross sections were calculated using different values of W_0. The results are shown in Figs. 4(a) and 4(b) for the two lowest energies, $E_{lab} = 24$ and 26 MeV, respectively. A comparison of the calculations with the best-fit imaginary potentials (solid lines) to the ones with $W_0 = 0$ (dash-dot lines) and an intermediate value (dashed lines) brings out the importance of using a nonzero imaginary potential to explain the elastic data at sub-barrier energies. A grid search on the radius and diffuseness parameters has been made to determine their sensitivities on the uncertainties on the imaginary potential. It was observed that a_w is sensitive even at the lowest energies. This finding is in contrast to the observation of Keeley *et al.* [4]. However, r_w was found to be less sensitive when compared to a_w and has a dominant contribution to the uncertainties on W.

B. Coupled-channels calculations and discussion

The continuum discretized coupled-channels (CDCC) method was employed using the code FRESCO [23] to calculate the cross sections for elastic and breakup channels and understand the energy dependence of the optical potentials. ^{6}Li was taken as a cluster of $\alpha + d$ for its bound as well as continuum (resonant and nonresonant) states. The breakup of the projectile into its fragments (α and d) is considered to be caused by inelastic excitations to different partial waves in the continuum, induced by the projectile fragments–target interactions due to Coulomb as well as nuclear forces.

The couplings that are included in the present calculations are similar to the ones described in our earlier paper [15]. For ^{6}Li, couplings to the 3^+ ($E_x = 2.18$ MeV), 2^+ ($E_x = 4.31$ MeV), and 1^+ ($E_x = 5.65$ MeV) resonant states as well as couplings to the nonresonant continuum were included. The continuum up to an excitation energy of 8 MeV with α-d relative momentum values $L = 0$, 1, and 2 were included in the coupling. For s and p waves, the continuum was discretized into 16 bins of equal width in the momentum of α-d relative motion. Three resonant states, with widths corresponding to 0.1, 2.0, and 3.0 MeV, respectively, were also treated as momentum bins, but with finer steps. In the presence of resonances for d waves, the discretization of the continuum was slightly modified in order to avoid double counting.

The couplings of the ground state to the continuum as well as continuum to continuum have been included. Reorientation coupling, i.e., the coupling of the quadrupole term of the projectile fragment–target potentials, was also incorporated. Since the inelastic cross section corresponding to the target excitation was found to be small, and the effect of its coupling on the elastic is known to be insignificant [24], no target excitation was included in the CDCC calculations.

The CDCC calculations were performed using the cluster-folded interaction [25], where α-target ($V_{\alpha+\mathrm{Bi}}$) and deuteron-target ($V_{d+\mathrm{Bi}}$) optical potentials were evaluated at $E_\alpha \approx \frac{2}{3}E_{^6\mathrm{Li}}$ and $E_d \approx \frac{1}{3}E_{^6\mathrm{Li}}$, respectively. Once a certain set of potential parameters for $V_{\alpha+\mathrm{Bi}}$ and $V_{d+\mathrm{Bi}}$ is chosen, there are no free parameters remaining in the model, except a possible overall renormalization factor [26]. The $V_{\alpha+\mathrm{Bi}}$ potential used in our calculations was taken from Ref. [27] for $E_{\mathrm{lab}} = 24.8$ MeV. Both the real and the imaginary potentials were of Woods-Saxon volume form and the parameters are as follows: $v_0 = 107.4$ MeV, $r_0 = 1.361$ fm, $a_0 = 0.578$ fm, $w = 13.5$ MeV, $r_w = 1.412$ fm, and $a_w = 0.299$ fm. Similarly, the $V_{d+\mathrm{Bi}}$ potential, with real parameters $v_0 = 100.2$ MeV, $r_0 = 1.15$ fm, and $a_0 = 0.973$ fm and imaginary parameters $w = 15.37$ MeV, $r_w = 1.45$ fm, and $a_w = 0.559$ fm, were taken to be the same as that of $d+^{208}$Pb at 12 MeV [28]. The imaginary parts of $V_{\alpha+\mathrm{Bi}}$ and $V_{d+\mathrm{Bi}}$ describe the removal of flux whenever the individual fragments themselves break up, excite, or fuse with the target. The strengths of the real part of $V_{\alpha+\mathrm{Bi}}$ as well as $V_{d+\mathrm{Bi}}$ have been adjusted by a scale factor of 0.8 to 1.0 compared to the values in Refs. [27,28] in order to explain the elastic data in the measured energy range of 24–50 MeV.

Results of the CDCC calculations with full (no) couplings for elastic scattering at all the measured energies ($E_{\mathrm{lab}} = 24$–50 MeV) are shown as dashed (dotted) lines in Fig. 2. It can be seen that the coupling of the breakup channels has a significant effect on elastic scattering. The effect of coupling of breakup channels with relative angular momentum $L = 2$ on elastic scattering is found to be the most dominant over the entire energy range, consistent with the observations made by Kelly *et al.* for the ^{6}Li + ^{208}Pb system [29]. The increase in elastic cross section at backward angles with breakup couplings implies that the real dynamic polarization potential (DPP) generated by these couplings must be repulsive in nature. The mean component of the DPP generated due to the couplings was calculated using FRESCO as described in Ref. [30] and its behavior around the surface region (11–15 fm) is shown in Fig. 5. At the strong absorption radius ($R_{\mathrm{sa}} = 12.4$ fm) and around the surface region, the real part of the DPP, i.e., ΔV_p, is indeed found to be highly repulsive (+ve) and the imaginary part of the DPP, i.e., ΔW_p, is attractive (−ve).

In Fig. 3, the average polarization potential (medium dashed line) along with the bare potential (short dashed line) is compared with the OM potential obtained from the elastic scattering fit. The real part of the polarization potential ΔV_p calculated at $r = 12.4$ fm was found to be positive at all the energies. It can be observed that the sum of the bare potential and the DPP, represented by the dash-dotted lines, reproduces the trend of experimental values (hollow circles) of both real and imaginary potentials. One can observe the trend of the imaginary part of the polarization potential particularly at energies below the barrier, where it becomes more and more attractive as we go down in energy and explains the energy dependence of the OM potential at this region.

C. Target inelastic and transfer channels

To see the effect of target inelastic states and transfer channels, coupled reaction channels (CRC) calculations

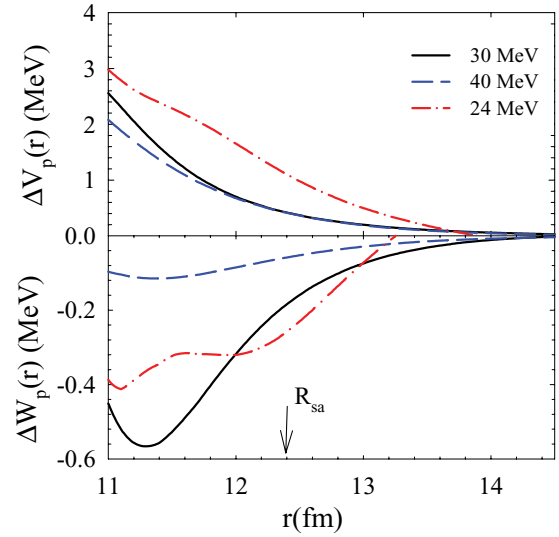

FIG. 5. (Color online) (a) Real part of the dynamic polarization potential ΔV_p around the strong absorption radius obtained from the coupled-channels calculations, using a cluster-folded potential, for 24 MeV (dash-dot line), 30 MeV (solid line), and 40 MeV (dashed line). (b) Same as (a) but for the imaginary potential.

are performed using the CDCC-derived effective potentials ($\Delta V_p + V_{\mathrm{bare}}$ and $\Delta W_p + W_{\mathrm{bare}}$, which includes the effect of projectile breakup) for the entrance channel. Similar to Ref. [3], we have coupled (i) 17 inelastic states corresponding to the multiplets of ^{208}Pb(3^- and 5^-)$\bigotimes \pi h_{9/2}$ and (ii) transfer couplings that include only low-lying excited states of the outgoing transfer partitions with six channels for 1-n pickup (^{7}Li + ^{208}Bi) and two channels each for 1-n stripping (^{5}Li + ^{210}Bi) and 1-p stripping (^{5}He + ^{210}Po) reactions. All the nonelastic channels are coupled to the entrance channel only. The inelastic states were treated as collective vibrational states and their form factors were chosen to be the derivatives of the potentials. The β values [31] and the deformation lengths are the same as those used in Ref. [3]. Reduced deformation lengths (Coulomb and nuclear) were calculated and used for each possible transition corresponding to the same collective vibrational states.

For transfer partitions, the real potentials were calculated using the semiemperical parametrization of folding model potentials given by Broglia and Winther [32]:

$$U_n(r) = -31.67\frac{R(A_1)R(A_2)}{R(A_1)+R(A_2)} \times \left[1+\exp\left(\frac{r-R(A_1,A_2)}{a}\right)\right]^{-1} \mathrm{MeV}, \quad (6)$$

where $R(A) = 1.233A^{\frac{1}{3}} - 0.98A^{-\frac{1}{3}}$ fm and $R(A_1, A_2) = R(A_1) + R(A_2) + \Delta R$ fm with the diffuseness parameter set to $a = 0.63$ fm and the free parameter $\Delta R = 0.2$ fm. The imaginary potential for the transfer channels were of Woods-Saxon squared form with a depth of 50 MeV, a radius parameter of 1.0 fm, and a diffuseness parameter of 0.4 fm. The potentials binding the transferred particles were of Woods-Saxon form, with radius $1.2A^{\frac{1}{3}}$ fm and diffuseness 0.6 fm, their depths being

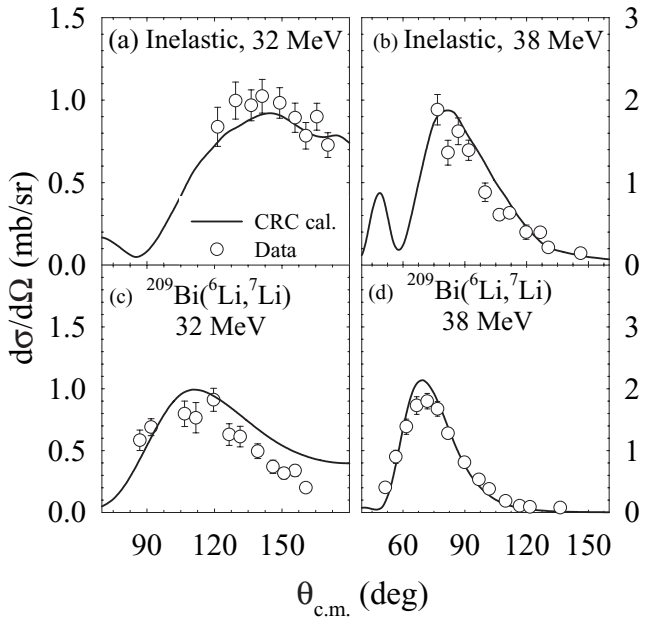

FIG. 6. Measured cross sections along with the CRC calculations for the target inelastic state (2.6 MeV) at $E_{\text{beam}} =$ (a) 32 and (b) 38 MeV. Cross sections for transfer reaction (^{6}Li,^{7}Li) at these energies are shown in (c) and (d), respectively (see text for details).

automatically adjusted to obtain the required binding energies. Spectroscopic factors are taken from the literature [3,33].

Typical results for inelastic states corresponding to $^{208}\text{Pb}(3^{-}) \bigotimes \pi h_{9/2}$ multiplets are compared with present data at 32 and 38 MeV in Figs. 6(a) and 6(b), respectively. Results for the transfer reaction ^{209}Bi(^{6}Li,^{7}Li) corresponding to ground state of ^{7}Li and the ground state plus first excited state of ^{208}Bi are compared with the present data in Figs. 6(c) and 6(d). A reasonable description of the above data along with elastic scattering ensures that the potential parameters used for CDCC calculations are not arbitrary rather they are highly restricted by the measured inelastic and transfer angular distributions. The effect of coupling of target inelastic states and transfer reactions on elastic scattering was found to be insignificant. So, the repulsive DPP generated in CDCC calculations due to breakup coupling seems to be the main reason for the absence of a normal threshold anomaly in the present system.

D. Fusion and reaction cross sections

In Fig. 7 we have compared the fusion cross sections calculated from the above CDCC calculations with the cross section data for CF (stars) [14], CF + ICF (thin "X") [14], and the total reaction (σ_R) obtained from the OM fit (hollow circles). Two methods were employed to calculate the fusion cross sections using the FRESCO code. The solid line corresponds to the results from the barrier penetration model (BPM) using the incoming wave boundary condition as done by Rusek *et al.* [34]; the dashed line represents the fusion simulated by cumulative absorption in a long-ranged imaginary potential. At energies above the Coulomb barrier, it is observed that the BPM fusion matches very well with the

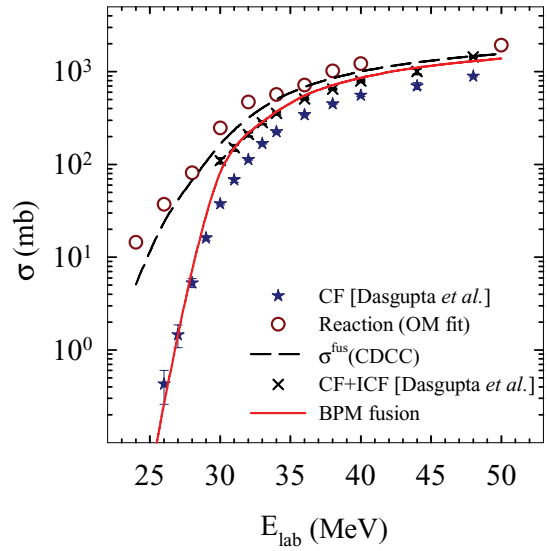

FIG. 7. (Color online) Fusion cross sections obtained from FRESCO by cumulative absorption (dashed line) and by barrier penetration model (solid line) compared with TF and CF data along with the OM-derived σ_R.

total fusion (TF = CF + ICF). But the CF data are found to be smaller by ∼30%–40%, which is in agreement with the conclusions drawn in Ref. [14]. However, at low energies, the CF data compare well with the calculated BPM fusion and show no suppression. Keeley *et al.* [35] have argued that it is not clear whether the fusion from the BPM should be compared with CF or TF. Since BPM assumes that all the flux that penetrates the Coulomb barrier, defined by the real part of the OM potential, leads to fusion, it may have contributions from both CF as well as ICF, and hence it may lead to higher BPM fusion than CF. However, this argument is not consistent with the observed behavior at low energies.

In a second method, the TF cross section is simulated by the cumulative absorption due to the long-ranged imaginary potential used in CDCC calculations. The total fusion thus predicted (dashed line) was found to overestimate the experimental data (denoted as "X") [14]. However, a good reproduction of elastic scattering data by the same CDCC calculations implies that the additional flux absorbed by the imaginary potential ($\sigma_{\text{abs}} - \sigma_{\text{TF}}$) must be equivalent to the sum of reaction cross sections of target-inelastic and transfer channels that are not included in the CDCC calculations.

E. Energy dependence of reaction channels

To find the relative contribution of the breakup channels to the total reaction cross section particularly at sub-Coulomb energies, the ratios of cross sections for breakup, CF, target inelastic, and transfer channels to σ_R are plotted as a function of energy in Fig. 8. At sub-barrier energies, it was interesting to observe that with decreasing energy, the CDCC calculated noncapture breakup cross section (solid line) increases, in contrast to the behavior of CF (stars), inelastic (dash-dot-dot line), and transfer (dashed line) cross sections. The transfer

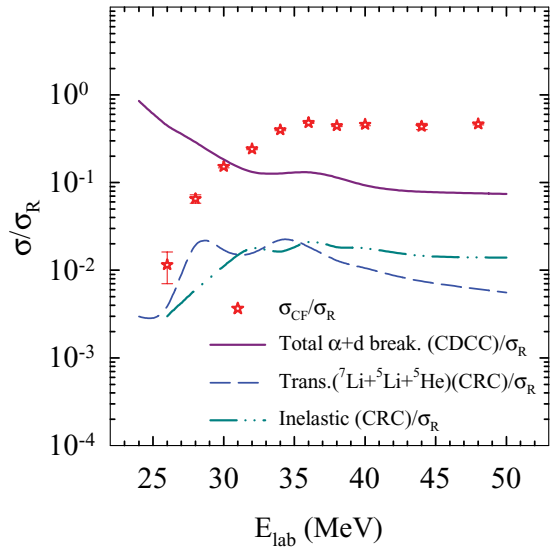

FIG. 8. (Color online) The ratios of cross sections for CF (σ_{CF}) data, calculated exclusive $\alpha + d$ breakup (σ^{excl}), target inelastic (σ^{inel}), and transfer (σ^{tr}) channels to total reaction cross section (σ_R) to show their relative contributions at different energies.

cross section represents the sum of the cross sections calculated for (^{6}Li,^{7}Li), (^{6}Li,^{5}Li), and (^{6}Li,^{5}He) channels. The above observation implies that when all the other channels start closing at sub-barrier energies, the breakup channel does not close, possibly due to the small breakup threshold energy of ^{6}Li, and the breakup can be caused by even Coulomb excitation. Thus it explains why the imaginary part of the optical potential does not vanish even much below the Coulomb barrier.

IV. SUMMARY AND CONCLUSIONS

In summary, the cross sections for elastic, inelastic, and transfer for the ^{6}Li + ^{209}Bi reaction have been measured at several energies around the Coulomb barrier. The conventional threshold anomaly was not observed in the energy dependence of the real potential obtained from the OM analysis. The imaginary part of the optical potential was observed to increase with decreasing energy below the Coulomb barrier. The bare plus polarization potential calculated from the CDCC calculations reproduces the trend of the energy dependence of both the real and imaginary potentials. The inelastic and transfer data that are explained simultaneously constrain the parameters used in the calculations.

The fusion cross section calculated by the BPM method reproduces the experimental total fusion (CF + ICF) at above barrier energies but underpredict it at sub-barrier energies. The TF cross section computed by the cumulative absorption in CDCC calculations was found to overestimate the experimental data. Since the CDCC calculations reproduce the elastic scattering data reasonably, the cumulative absorption cross section must be equal to the sum of TF and the reaction cross sections corresponding to the target-inelastic and transfer channels that are not included in the CDCC calculations.

The comparison of the probabilities of fusion, breakup, inelastic, and transfer reactions reveals that breakup dominates at sub-barrier energies and it behaves differently from others. While all the other channels effectively get closed, the breakup channel does not. The existence of a large breakup probability in this region does not allow the imaginary part of the optical potential to vanish.

The present results are very important for further understanding and development of theories based on a realistic model of breakup for the reactions involving weakly bound projectiles.

ACKNOWLEDGMENTS

We thank Dr. R. K. Choudhury for his keen interest and useful discussions on this work. Thanks are also due to the pelletron crew for the smooth operation of the accelerator during the experiments.

[1] C. Mahaux, H. Ng, and G. R. Satchler, Nucl. Phys. A **449**, 354 (1986).
[2] S. Santra, P. Singh, S. Kailas, A. Chatterjee, A. Shrivastava, and K. Mahata, Phys. Rev. C **64**, 024602 (2001).
[3] S. Santra, P. Singh, S. Kailas, A. Chatterjee, A. Navin, A. Shrivastava, A. M. Samant, and K. Mahata, Phys. Rev. C **60**, 034611 (1999), and references therein.
[4] N. Keeley, S. J. Bennett, N. M. Clarke, B. R. Fulton, G. Tungate, P. V. Drumm, M. A. Nagarajan, and J. S. Lilley, Nucl. Phys. A **571**, 326 (1994).
[5] A. M. M. Maciel *et al.*, Phys. Rev. C **59**, 2103 (1999).
[6] F. A. Souza, L. A. S. Leal, N. Carlin, M. G. Munhoz, R. Liguori Neto, M. M. de Moura, A. A. P. Suaide, E. M. Szanto, A. Szanto de Toledo, and J. Takahashi, Phys. Rev. C **75**, 044601 (2007).
[7] A. Pakou *et al.*, Phys. Rev. C **69**, 054602 (2004).
[8] C. Signorini *et al.*, Phys. Rev. C **61**, 061603(R) (2000).
[9] S. B. Moraes, P. R. S. Gomes, J. Lubian, J. J. S. Alves, R. M. Anjos, M. M. Sant Anna, I. Padron, and C. Muri, Phys. Rev. C **61**, 064608 (2000).
[10] P. R. S. Gomes *et al.*, Phys. Rev. C **71**, 034608 (2005).
[11] M. S. Hussein, P. R. S. Gomes, J. Lubian, and L. C. Chamon, Phys. Rev. C **73**, 044610 (2006).
[12] R. J. Woolliscroft, B. R. Fulton, R. L. Cowin, M. Dasgupta, D. J. Hinde, C. R. Morton, and A. C. Berriman, Phys. Rev. C **69**, 044612 (2004).
[13] L. F. Canto, P. R. S. Gomes, R. Donangelo, and M. S. Hussein, Phys. Rep. **424**, 1 (2006).
[14] M. Dasgupta *et al.*, Phys. Rev. C **70**, 024606 (2004).
[15] S. Santra, V. V. Parkar, K. Ramachandran, U. K. Pal, A. Shrivastava, B. J. Roy, B. K. Nayak, A. Chatterjee, R. K. Choudhury, and S. Kailas, Phys. Lett. B **677**, 139 (2009).
[16] A. Gomez Camacho, P. R. S. Gomes, and J. Lubian, Phys. Rev. C **82**, 067601 (2010).

[17] N. Keeley, J. M. Cook, K. W. Kemper, B. T. Roeder, W. D. Weintraub, F. Marechal, and K. Rusek, Phys. Rev. C **68**, 054601 (2003).
[18] A. F. Zeller, D. C. Weisser, T. R. Ophel, and D. F. Hebbard, Nucl. Phys. A **332**, 515 (1979).
[19] G. R. Satchler and W. G. Love, Phys. Rep. **55**, 183 (1979).
[20] J. Cook, Comput. Phys. Commun. **25**, 125 (1982).
[21] C. W. De Jager *et al.*, At. Data Nucl. Data Tables **14**, 479 (1974).
[22] G. R. Satchler, Phys. Rep. **199**, 147 (1991).
[23] I. J. Thompson, Comput. Phys. Rep. **7**, 167 (1988).
[24] K. Rusek, J. Gmez-Camacho, I. Martel-Bravo, and G. Tungate, Nucl. Phys. A **614**, 112 (1997).
[25] F. G. Perey and G. R. Satchler, Nucl. Phys. A **97**, 515 (1967).
[26] Y. Hirabayashi and Y. Sakuragi, Phys. Lett. B **258**, 11 (1991).
[27] P. Singh, A. Chatterjee, S. K. Gupta, and S. S. Kerekatte, Phys. Rev. C **43**, 1867 (1991).
[28] P. R. Christensen, A. Berinde, I. Neamu, and N. Scintei, Nucl. Phys. A **129**, 337 (1969).
[29] G. R. Kelly *et al.*, Phys. Rev. C **63**, 024601 (2000).
[30] I. J. Thompson, M. A. Nagarajan, J. S. Lilley, and M. J. Smithson, Nucl. Phys. A **505**, 84 (1989).
[31] T. P. Cleary, N. Stein, and P. R. Maurenzig, Nucl. Phys. A **232**, 287 (1974).
[32] R. A. Broglia and A. Winther, *Heavy Ion Reactions*, Parts I and II (Addison-Wesley, Redwood City, CA, 1991).
[33] P. L. Kerr, K. W. Kemper, P. V. Green, K. Mohajeri, E. G. Myers, and B. G. Schmidt, Phys. Rev. C **55**, 2441 (1997).
[34] K. Rusek, N. Alamanos, N. Keeley, V. Lapoux, and A. Pakou, Phys. Rev. C **70**, 014603 (2004).
[35] N. Keeley, R. Raabe, N. Alamanos, and J. L. Sida, Prog. Part. Nucl. Phys. **59**, 579 (2007).